A global relationship between the ocean water cycle and near-surface salinity

Lisan Yu[1]

Received 31 December 2010; revised 21 July 2011; accepted 21 July 2011; published 18 October 2011.

[1] Ocean evaporation (E) and precipitation (P) are the fundamental components of the global water cycle. They are also the freshwater flux forcing (i.e., E-P) for the open ocean salinity. The apparent connection between ocean salinity and the global water cycle leads to the proposition of using the oceans as a rain gauge. However, the exact relationship between E-P and salinity is governed by complex upper ocean dynamics, which may complicate the inference of the water cycle from salinity observations. To gain a better understanding of the ocean rain gauge concept, here we address a fundamental issue as to how E-P and salinity are related on the seasonal timescales. A global map that outlines the dominant process for the mixed-layer salinity (MLS) in different regions is thus derived, using a lower-order MLS dynamics that allows key balance terms (i.e., E-P, the Ekman and geostrophic advection, vertical entrainment, and horizontal diffusion) to be computed from satellite-derived data sets and a salinity climatology. Major E-P control on seasonal MLS variability is found in two regions: the tropical convergence zones featuring heavy rainfall and the western North Pacific and Atlantic under the influence of high evaporation. Within this regime, E-P accounts for 40–70% MLS variance with peak correlations occurring at 2–4 month lead time. Outside of the tropics, the MLS variations are governed predominantly by the Ekman advection, and then vertical entrainment. The study suggests that the E-P regime could serve as a window of opportunity for testing the ocean rain gauge concept once satellite salinity observations are available.

Citation: Yu, L. (2011), A global relationship between the ocean water cycle and near-surface salinity, *J. Geophys. Res.*, *116*, C10025, doi:10.1029/2010JC006937.

1. Introduction

[2] Evaporation from the ocean and precipitation to the ocean are the primary source (86%) and sink (78%) of atmospheric water vapor and, accordingly, the major contributors to our planet's hydrological cycle [*Baumgartner and Reichel*, 1975; *Schmitt*, 2008]. Over the open ocean away from the coastal regions and high latitudes, impacts of river runoff and ice melting are limited and evaporation-minus-precipitation (referred to as E-P thereafter) is the major freshwater flux forcing that, together with dynamical processes in the ocean, drives the variability of ocean salinity. The profound effects of a changing salinity on ocean mixing, water mass formation, and ocean general circulation have been reported in many observational studies [e.g., *Dickson et al.*, 1988; *Lukas and Lindstrom*, 1991; *Curry et al.*, 2003; *Boyer et al.*, 2005].

[3] It has long been known that, on a long-term mean basis, the spatial distribution of the near-surface salinity is closely related to the spatial pattern of E-P. High salinities are located in the subtropical oceans where evaporation exceeds precipitation, and low salinities are located in the tropical and high latitudes where precipitation exceeds evaporation. Given that ocean salinity is a better observed variable than evaporation and/or precipitation, the concept of using the oceans as a rain gauge for the global water cycle has been proposed. Several attempts have been made in past decades. For instance, *Elliott* [1974] used data collected during the Barbados Oceanographic and Meteorological Experiment (BOMEX) in the summer of 1969 and attempted to evaluate the total precipitation from the observed salinity changes. However, the results were inconclusive. In the absence of rain events, the change of the salinity within the top 10 m is at the same magnitude as the salinity fluctuation caused by the dilution of rainfall (0.15 psu). Some experiments were also performed during the TOGA COARE field program in the western tropical Pacific [*Webster and Lukas*, 1992], showing that the accumulated rainfall can be estimated with the same uncertainty as that obtained from various conventional and radar rain measurements [*Short et al.*, 1997; *Wijesekera et al.*, 1999]. More recently, *Yaremchuk* [2006] attempted to improve the monthly precipitation climatology in the monsoon heavy-

[1]Department of Physical Oceanography, Woods Hole Oceanographic Institution, Woods Hole, Massachusetts, USA.

0148-0227/11/2010JC006937

rain regions by enforcing the surface salinity climatology of the World Ocean Atlas 2005 (WOA05 [*Antonov et al.*, 2006]) as a constraint for an ocean model. By assuming that the model errors are much smaller than the forcing errors, he suggested that a SSS accuracy of 0.1–0.2 psu is sufficient to constrain the monthly precipitation estimates in the heavy rainfall regions such as the Bay of Bengal.

[4] The promise of using ocean salinity observations to understand the change in the ocean water cycle has gained increasing attention in recent years. There are two main drivers behind this trend. One is the rapid expansion of the salinity archive, thanks to the technology advancement and extensive international collaborations that have significantly advanced in situ and satellite observing systems. The other driver is the need to better understand and quantify the change of the global water cycle in a changing climate. There are currently more than 3,200 ARGO free-floating profiling floats distributed throughout the world's oceans, providing temperature and salinity profiles around the globe for the past ten years [*Riser et al.*, 2008; *Roemmich et al.*, 2009]. There are also two salinity satellite missions. One is the Soil Moisture and Ocean Salinity Mission (SMOS) by the European Space Agency [*Berger et al.*, 2002], which was launched in November 2009 and has begun its operational life transmitting data. The other is the NASA Aquarius mission [*Lagerloef et al.*, 2008], which was launched in June 2011 aboard the Argentine SAC-D spacecraft. The two salinity missions will deliver global sea surface salinity (SSS) measurements with 150-km spatial resolution on a 30-day time scale and a measurement error less than 0.2 psu.

[5] Compared to the rapidly growing salinity measurements, the progress made in observing the global hydrological components, particularly ocean evaporation and precipitation, has not been as rapid. Retrieving evaporation directly from a satellite is still not achievable, and observing sea-surface evaporation directly from in situ instruments is in the experimental stage. At present, ocean evaporation is constructed from air-sea observables (such as wind speed, air/sea temperature and humidity, sea level pressure) using bulk flux algorithms [*Fairall et al.*, 2003]. The different input data sources, the various treatments of the near-surface air humidity/temperature that is not provided by satellite, and/or the different flux parameterizations have led to a large spread in the estimates of global ocean evaporation fields [*Yu et al.*, 2007; *Andersson et al.*, 2011]. In some regions such as the tropical Indian Ocean and the south oceans, the differences between the products are larger than the absolute mean value. The situation for quantifying the precipitation over the oceans is equally unsatisfactory, due to the lack of sufficient ground-based measurements to calibrate the algorithms for retrieving rain rate from either radar precipitation measurements or visible (VIS)-infrared (IR) and passive microwave (PMW) observations [*Gruber and Levizzani*, 2008]. Apparently, there is the need of developing new and innovative approaches to improve the estimates of evaporation and precipitation. Satellite salinity mission is also a water balance mission. The monitoring of surface salinity from space, together with the provision of regular surface and sub-surface salinity profiles from in situ observing systems, provides not only a key constraint on the balance of the freshwater input over the ocean, but also a valid reference measure to understand the strength of the water cycle. It appears that the time is ripe to revisit the concept of the ocean rain gauge and to define new steps toward its realization. The present study aims at this direction.

[6] Linking the salinity information to E-P is challenging, because salinity and E-P are related through complex upper ocean dynamics. Unlike surface heat flux that serves as both forcing and damping mechanisms for sea surface temperature (SST) [*Frankignoul*, 1985], E-P forces salinity anomalies but does not damp them. Salinity anomalies tend to be more persistent than SST, and are more strongly influenced by oceanic advection/mixing [*Spall*, 1993; *Hall and Manabe*, 1997; *Mignot and Frankignoul*, 2003, 2004]. The important role of the advection processes in governing the regional salinity has been documented by many studies [e.g., *Delcroix and Hénin*, 1991; *Johnson et al.*, 2002; *Rao and Sivakumar*, 2003; *Reverdin et al.*, 2007; *Foltz and McPhaden*, 2008; *Ren and Riser*, 2009; *Bingham et al.*, 2010]. Yet, there are also numerous studies showing the dominance of E-P on near-surface salinity variations in the tropical oceans [e.g., *Delcroix et al.*, 1996; *Boyer and Levitus*, 2002; *Foltz and McPhaden*, 2008; *Bingham et al.*, 2010]. For instance, *Delcroix and Hénin* [1991] analyzed the salinity measurements acquired along the tropical Pacific ship-of-opportunity tracks and showed that more than 40% of seasonal salinity variability in the Intertropical Convergence Zone (ITCZ) can be attributed to the E-P forcing. *Cravatte et al.* [2009] showed that the observed surface freshening in the tropical western Pacific Ocean during 1955–2003 was driven by an increase of precipitation associated with ITCZ. The ITCZ is a region of deep upward convection, with precipitation far exceeding evaporation. In addition, the mixed layer depth (denoted by h) is characteristically shallower in the tropical oceans due to a stronger upper-ocean density stratification [*de Boyer Montégut et al.*, 2004] so that the effective E-P forcing (i.e., $(E\text{-}P)/h$) is larger.

[7] The likely existence of a high correlation between the changes in E-P and salinity indicates that there might be a region where the change in local salinity is influenced primarily by E-P. If so, this region could serve as a test bed for initial implementation of the ocean rain gauge concept. However, where this E-P dominant regime exists and how to identify such regime over the global scale remain unknown. These questions need to be addressed before a concrete strategy can be formulated. In this study, an attempt is made to examine these questions through applying a data analysis approach to the mixed-layer salinity (MLS) budget equation. In particular, the study is to quantify key balance processes in the MLS budget, and to identify the E-P dominance regime through a covariance analysis of the relative contribution of E-P versus oceanic processes to MLS variability. It should be noted that although many satellite-derived data sets are available, they are still insufficient to fully resolve all processes (such as frontal mixing, shear instabilities) in the MLS budget equation. Thus, the present study is based on a lower-order dynamics of the MLS budget equation and provides a first-order characterization of the key processes governing the MLS. In addition, the historical distribution of near-surface salinity observations is gener-

ally sparse and does not have adequate temporal or spatial resolution to resolve salinity variability at various time scales. The present study focuses on the seasonal relationship between the MLS and *E-P* by utilizing the salinity climatology from WOA05.

[8] Seasonal variability of near-surface salinity has been examined by many studies, using either the gridded WOA [e.g., *Boyer and Levitus*, 2002; *Rao and Sivakumar*, 2003; *Dong et al.*, 2009] or in situ database in better sampled regions/locations [e.g., *Delcroix and Hénin*, 1991; *Dessier and Donguy*, 1994; *Donguy and Meyers*, 1996; *Delcroix et al.*, 1996; *Cronin and McPhaden*, 1998; *Johnson et al.*, 2002; *Foltz and McPhaden*, 2008; *Reverdin et al.*, 2007; *Ren and Riser*, 2009; and *Bingham et al.*, 2010]. The present study benefits particularly from the basin-scale studies by *Boyer and Levitus* [2002] and *Bingham et al.* [2010]. These two studies provided a comprehensive description of seasonal amplitudes and phases of the mixed layer salinity, *E-P*, and/or the horizontal advection from the viewpoint of harmonic analysis. They are a useful validation for the present study that is based on a covariance analysis and has an objective of obtaining a big picture of the global *E-P* dominance on seasonal time scales.

[9] The presentation is organized as follows. Description of the mixed layer model and data is given in section 2, in which seasonal variations of all the terms included in the model are also presented. The covariance analysis of each of the processes contributing to seasonal salinity variability is shown in section 3. The global relationship between *E-P* and salinity changes is discussed in section 4. Important findings are summarized in section 5.

2. Dynamics of Seasonal Variations of the Mixed Layer Salinity

2.1. Governing Equations

[10] The mixed layer in use is represented as a slab of seawater with uniform properties from the surface to the bottom. Following *Mignot and Frankignoul* [2003], the vertically integrated equation for the MLS can be written as

$$h\frac{\partial S}{\partial t} = S_0(E-P) - \boldsymbol{U}\cdot\nabla S - \Gamma(w_e)(S-S_b) + h\kappa\nabla^2 S \quad (1)$$

where S_0 denotes the mean surface salinity, E evaporation, P precipitation, h the mixed-layer depth, $\boldsymbol{U}$ the horizontal transport in the mixed layer, w_e the entrainment velocity at depth $z = h$, S_b the salinity just below h, Γ the Heaviside function, and κ the horizontal mixing coefficient. Effect of river runoff is not considered in this study.

[11] The horizontal transport $\boldsymbol{U}$ can be separated into an Ekman component $\boldsymbol{U}_{EK}$, which is driven by wind stress $\boldsymbol{\tau}$, and a geostrophic component $\boldsymbol{U}_g$, which is governed by horizontal gradient in density. By doing so, the equation for $\boldsymbol{U}$ is expressed as

$$\boldsymbol{U} = \boldsymbol{U}_{EK} + \boldsymbol{U}_g = \frac{\boldsymbol{\tau}\times\boldsymbol{k}}{\rho f} + \frac{hg\nabla\eta\times\boldsymbol{k}}{f} \quad (2)$$

where g is the acceleration of gravity, f the Coriolis frequency, and η the sea surface elevation.

[12] The entrainment velocity w_e in equation (1) consists of vertical Ekman velocity w_{EK} and the h tendency:

$$w_e = w_{EK} + \left(\frac{\partial h}{\partial t} + \nabla\cdot h\boldsymbol{U}\right) = \frac{\nabla\times\boldsymbol{\tau}}{\rho f} + \left(\frac{\partial h}{\partial t} + \nabla\cdot h\boldsymbol{U}\right) \quad (3)$$

The Ekman vertical velocity w_{EK} corresponds to the upwelling/downwelling generated by the convergence/divergence of the horizontal Ekman transport. The h tendency term represents the integrated effects of the changing wind, surface buoyancy flux, and turbulent dissipation [*Niiler and Kraus*, 1977]. The Heaviside function Γ is introduced because the entrainment and detrainment are treated separately. The entrainment of subsurface stratified water affects MLS whereas the detrainment of the mixed layer water to the subsurface does not change MLS [*Kraus and Turner*, 1967].

[13] Each field is decomposed into an annual mean (denoted by an overbar) and the departure from the mean (denoted by a prime). If the contributions from the mean products of anomalies are neglected, the equation for the MLS seasonal anomalies is written as

$$\frac{\partial S'}{\partial t} \approx \underbrace{\frac{S_0(E'-P')}{\overline{h}}}_{\text{(a)}} \underbrace{-\overline{\boldsymbol{U}}\cdot\nabla S'}_{\text{(b)}} \underbrace{-\boldsymbol{U}'\cdot\nabla\overline{S}}_{\text{(c)}} \underbrace{-\frac{(\Gamma(w_e)(S-S_b))'}{\overline{h}}}_{\text{(d)}} \underbrace{+\kappa\nabla^2 S'}_{\text{(e)}} \underbrace{}_{\text{(f)}} \quad (4)$$

Term a is the rate of change of the MLS anomaly, term b is the change of the MLS anomaly by the effective *E-P* anomaly, term c represents advection of the MLS anomaly by mean currents, term d denotes advection of the mean MLS by anomalous currents, term e is the entrainment/detrainment of the MLS through the base of the mixed layer, and term f represents horizontal mixing. For term f, a Laplacian horizontal diffusion with a coefficient κ (set to 500 ms^{-2}) is used to represent sub-scale ed6dy advection.

[14] Equation (4) represents a lower-order dynamical description of seasonal variations of the MLS. The advantage of using this equation is that the key balance terms can all be computed from existing data sets.

2.2. Data

[15] To compute the terms a–f in equation (4), data fields of S, S_b, h, P, E, $\boldsymbol{\tau}$, and η are needed. The respective data sources are listed below.

[16] 1. The mixed-layer depth (h) was derived from the WOA05 1° × 1° monthly temperature and salinity fields using a density criterion, i.e., h is determined as the depth at which density is 0.125 kg m^{-3} higher than the surface density [*de Boyer Montégut et al.*, 2004]. The salinity averaged within h is taken as the MLS (S), and the subsurface salinity S_b is chosen as the salinity 20 m below the mixed layer depth.

[17] 2. Altimeter measurements of sea surface height from *AVISO* [2009] are sea level (η) anomalies with respect to a long-term mean; and they were a base data set for computing the geostrophic current anomalies. To obtain the mean global geostrophic currents, we introduced the time-averaged (1992–2002) global sea level developed from a joint analysis of drifter, satellite altimeter, wind, and the

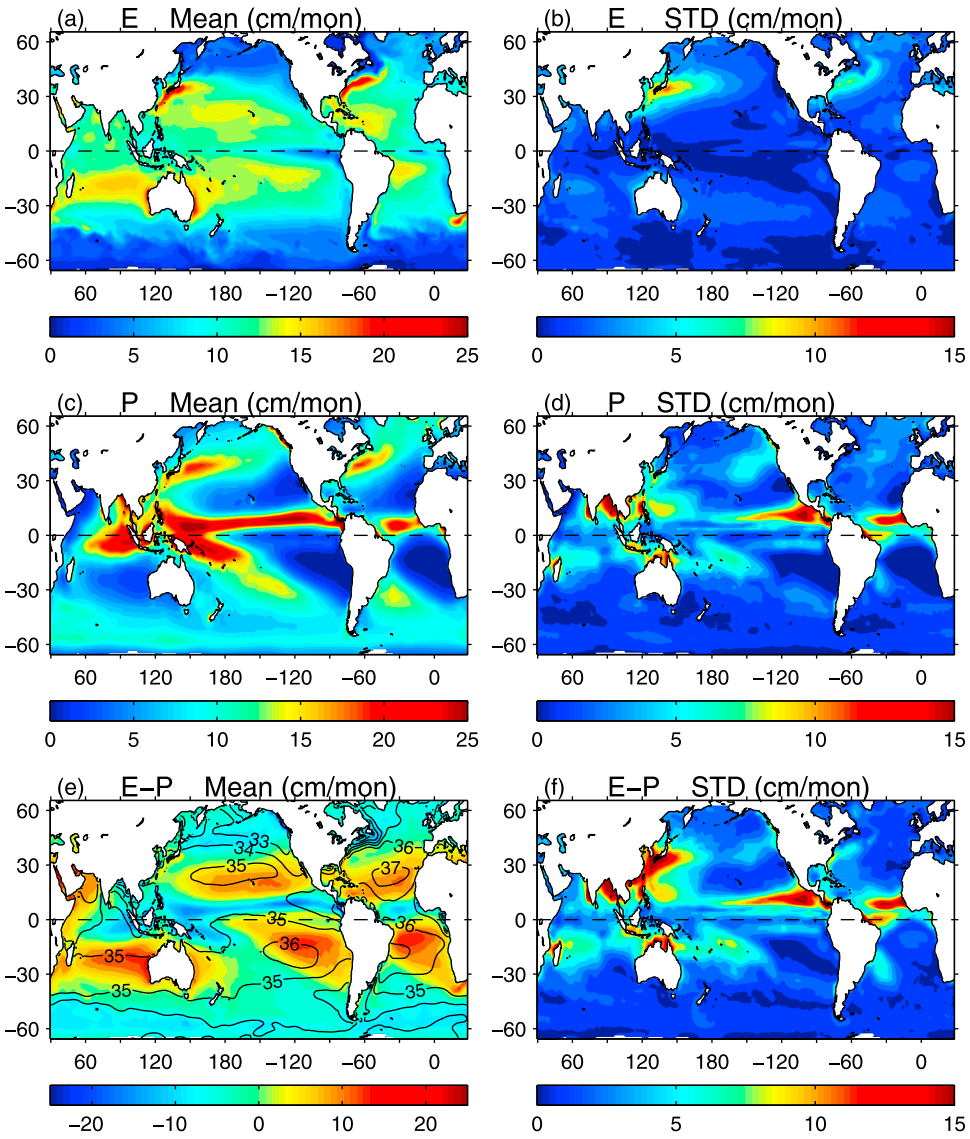

Figure 1. Annual mean and seasonal STD fields (a and b) for *E*, (c and d) for *P*, and (e and f) for *E*-*P*. Contours of the annual-mean MLS field are superimposed in Figure 1e.

GRACE Gravity Model-01 data by *Niiler et al.* [2003] and *Maximenko et al.* [2009]. The two data sets, both gridded onto 0.5° boxes, are averaged onto the 1° × 1° WOA grids.

[18] 3. The monthly satellite-gauge merged precipitation (*P*) analysis from the Global Precipitation Climatology Project (GPCP) Version 2.1 [*Adler et al.*, 2003] was obtained. The version 2.1 data are a combination of microwave (MW) precipitation estimates from Special Sensor Microwave Imager (SSM/I) emission and scattering algorithms, and infrared (IR) estimates primarily from geostationary satellites (United States, Europe, Japan), and secondarily from polar-orbiting satellites (United States). Additional low-Earth orbit estimates include the Atmospheric Infrared Sounder (AIRS data from the NASA Aqua, and Television Infrared Observation Satellite Program (TIROS) Operational Vertical Sounder (TOVS) and Outgoing Longwave Radiation Precipitation Index (OPI) data from the NOAA series satellites. The merging approach takes advantage of the strength of each data source and results in a final monthly product on a 2.5° × 2.5° grid that covers the period from January 1979 to June 2009.

[19] 4. The evaporation (*E*) data set was taken from the Version 3 products of the Objectively Analyzed air-sea Fluxes (OAFlux) project [*Yu and Weller*, 2007; *Yu et al.*, 2008]. Similar to the strategy adopted by GPCP, the OAFlux global analysis employs an objective synthesis that seeks the best-possible estimates for surface meteorological variables through combining satellite observations. Three atmospheric reanalyses were included in the synthesis to provide the information of near-surface air temperature and humidity that is not measured by satellites. The optimally determined surface meteorological variables are then used as inputs to the 3.0 b bulk flux algorithm of the Coupled Ocean-Atmosphere Response Experiment (COARE) [*Fairall et al.*, 2003] to compute the ocean evaporation. The OAFlux 1° gridded analysis covers the period from January 1958 onward.

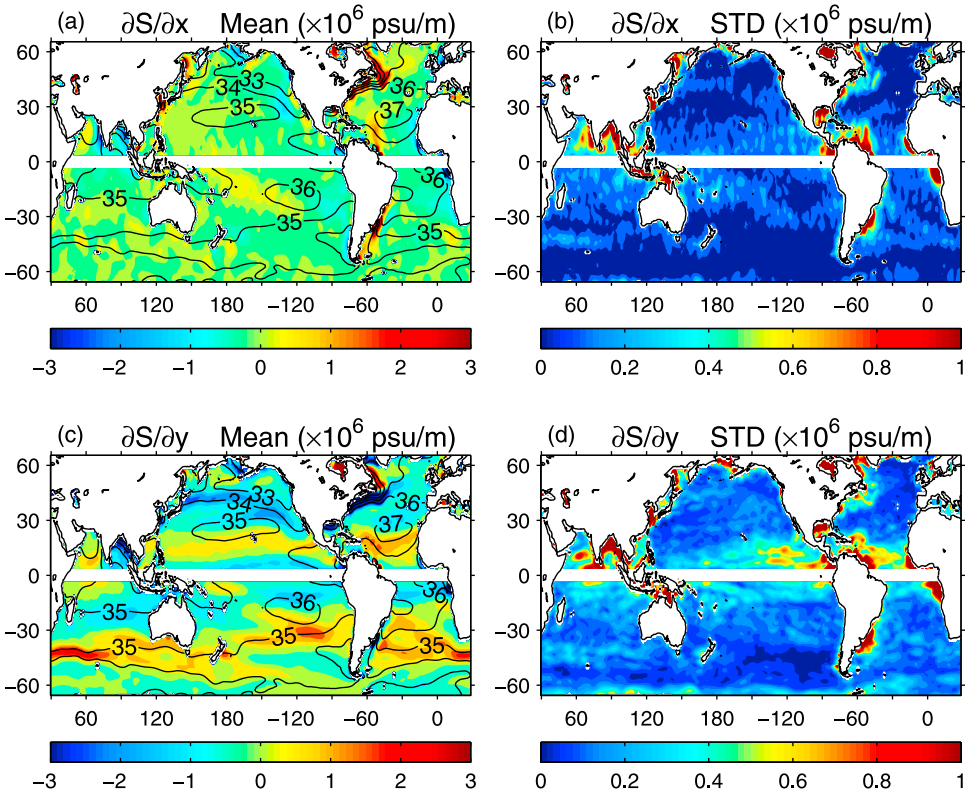

Figure 2. Annual mean and seasonal STD fields for salinity gradient fields (a and b) for zonal MLS gradient ($\partial S/\partial x$) and (c and d) for meridional MLS gradient ($\partial S/\partial y$). Contours of the annual-mean MLS field are superimposed onto Figures 2a and 2c.

[20] 5. The wind stress (τ) data set was taken from the OAFlux newly developed satellite-based, 0.25° gridded, daily global vector wind analysis [*Yu and Jin*, 2011]. This product is a synergy of microwave radiometric wind speed measurements (from SSM/I and Advanced Microwave Scanning Radiometer for Earth Observing System (AMSR-E)) and scatterometer vector wind measurements (from QuikSCAT and ASCAT). Wind directions from three atmospheric reanalyses were used as initial assignments in developing vector wind analysis for the period from July 1987 to August 1999, during which only wind speed measurements from SSM/I are available. The wind directions are adjusted iteratively by a least squares fitting to the data constraints and the imposed kinematic properties. The OAFlux wind stress time series is presently available from July 1987 to present.

[21] The time series of P, E, and τ overlap during the 21-year period from January 1988 to December 2008, and hence, this period was used to construct the monthly climatology. The spatial resolution is set on the 1° × 1° grid of the WOA05 climatology. The OAFlux E is already 1° gridded. The 2.5° gridded GPCP P was linearly interpolated, and the 0.25° gridded OAFlux τ was 16-point averaged to produce the 1° gridded field. The SSH climatology was constructed over the period from 1993 to 2008.

2.3. Seasonal Variations in Input Data Fields

2.3.1. *E*, *P*, and *E-P*

[22] The annual mean and seasonal standard deviations (STD) for E, P, and E-P fields are shown in Figures 1a–1f, respectively. On the annual-mean basis, large E can be found in two general areas [*Yu*, 2007]. One area is the global western boundary current (WBC) regions, the most noted of which are the Gulf Stream (GS) off the United States, and the Kuroshio and its Extension (KE) off Japan; and the other area is the broad northern and southern subtropical oceans (Figure 1a). By comparison, large P is located predominantly in regions of intense tropical convergence [*Adler et al.*, 2003], such as the ITCZ and the South Pacific convergence zone (SPCZ). Sufficiently large P is also observed along the midlatitude storm tracks off the east coast of Asia and North America (Figure 1c). Over the global scale, the maximum centers of E and P do not usually collocate, except for the WBC regions in the Northern Hemisphere where large P associated with the midlatitude storm tracks is slightly downstream of the E maxima, which leads to a compensation between E and P and thus a weak E-P (Figure 1e). On top of the annual mean E-P pattern, contours of the surface salinity from WOA are superimposed. The close relationship between E-P and surface salinity is clearly displayed, with high salinities in regions of excessive evaporation and low salinities in regions of excessive precipitation. It is also noted that in each ocean basin, the subtropical salinity maxima are centered near 20–25° in latitude, while net evaporation maxima are located near 15° in latitude. The poleward displacement of the salinity maxima is attributed to the meridional advection and vertical mixing.

[23] The pattern of seasonal STD of E (Figure 1b) is different from its annual-mean pattern. Significant seasonal

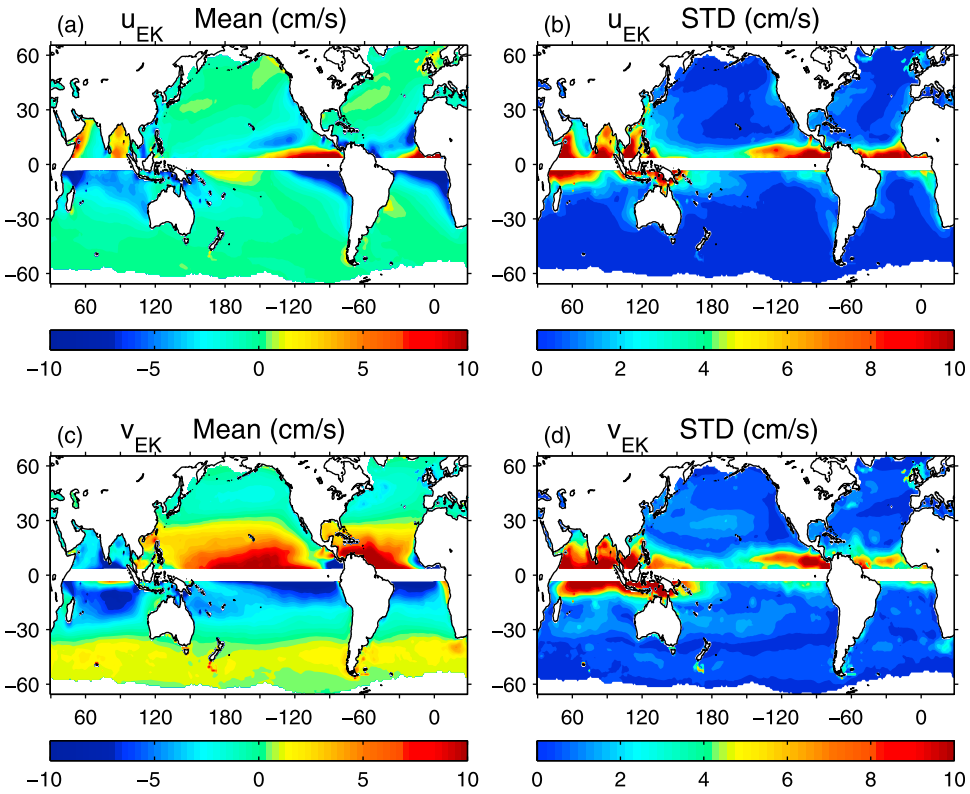

Figure 3. Annual mean and seasonal STD fields (a and b) for zonal Ekman velocity (u_{EK}) and (c and d) for meridional Ekman velocity (v_{EK}).

variability appears in the WBC regions, with large values occurring predominantly in the KE region and secondarily in the GS region. The magnitude of STD over KE exceeds 10 cm/mon, which is about half of its annual-mean value. This large seasonal variability is due to the strong influence of the East Asian monsoon [*Chang et al.*, 2004]. The annually reversal monsoon winds bring a warm and wet summer and a cold and dry winter to the region, resulting in significant seasonal changes in air-sea latent heat exchange. Evaporation over the broad subtropical oceans is intense throughout the year, but shows no significant seasonal variability.

[24] On the other hand, the pattern of seasonal STD of P (Figure 1d) has a broad resemblance to its annual mean pattern. Significant STD occur in the tropical rain belt, with peak values greater than 10 cm/mon appearing in the Bay of Bengal, the western tropical north Pacific, the eastern tropical north Pacific, and the tropical north Atlantic. The seasonal changes of P in these regions are primarily the result of the meridional migration of ITCZ with seasons. Significant STD of P, with magnitude of 5 cm/mon, are also seen in SPCZ and the southwestern subtropical Indian Ocean.

[25] The STD pattern of E-P (Figure 1f) shows that seasonal variations of P dominate the tropical oceans, while seasonal variations of E are relatively weaker with noticeable contributions only in the vicinity of the WBCs, particularly the KE region. The latter connects in its south with the area of significant STD of P in the western tropical north Pacific, forming a broad area of large E-P variability on the seasonal timescale. In general, the seasonal variance of E-P are more prominent in the northern oceans than in the southern oceans, and more pronounced in mid and low latitudes than at higher latitudes.

2.3.2. MLS and Horizontal Salinity Gradients

[26] The annual-mean pattern and seasonal STD of the zonal and meridional gradients of the MLS are shown in Figures 2a–2d. For the salinity zonal gradient $\partial S/\partial x$, a positive (negative) sign denotes a higher salinity in the east (west). For the salinity meridional gradient $\partial S/\partial y$, a positive sign (negative) denotes a higher salinity in the north (south). The salinity gradients are a measure of the direction and intensity of the horizontal salinity advection due to currents.

[27] Large salinity gradients exist near the coastal regions, particularly in the northern hemisphere, which appear to be influenced by the freshwater influx from runoff. In the open oceans away from these boundaries, the mean $\partial S/\partial x$ (Figure 2a) is mostly negative and weak, and the seasonal STD are also weak (Figure 2b). By comparison, the magnitude of the mean $\partial S/\partial y$ is about one order larger than the magnitude of the mean $\partial S/\partial x$ (Figure 2c). Additionally, the spatial structure of the mean $\partial S/\partial y$ is dominated by the broad zonally oriented bands with alternating positive and negative values. Two positive zonal bands are noteworthy; one is confined between 10 and 20°N in the northern oceans and the other is in the southern oceans with a center around 40°S. The two positive bands are both located south of the subtropical salinity maximum centers, delineating that positive meridional gradients represent higher salinities in the north. Significant seasonal variance of $\partial S/\partial y$ (Figure 2c) is seen in the tropical oceans, particularly in the eastern north tropical

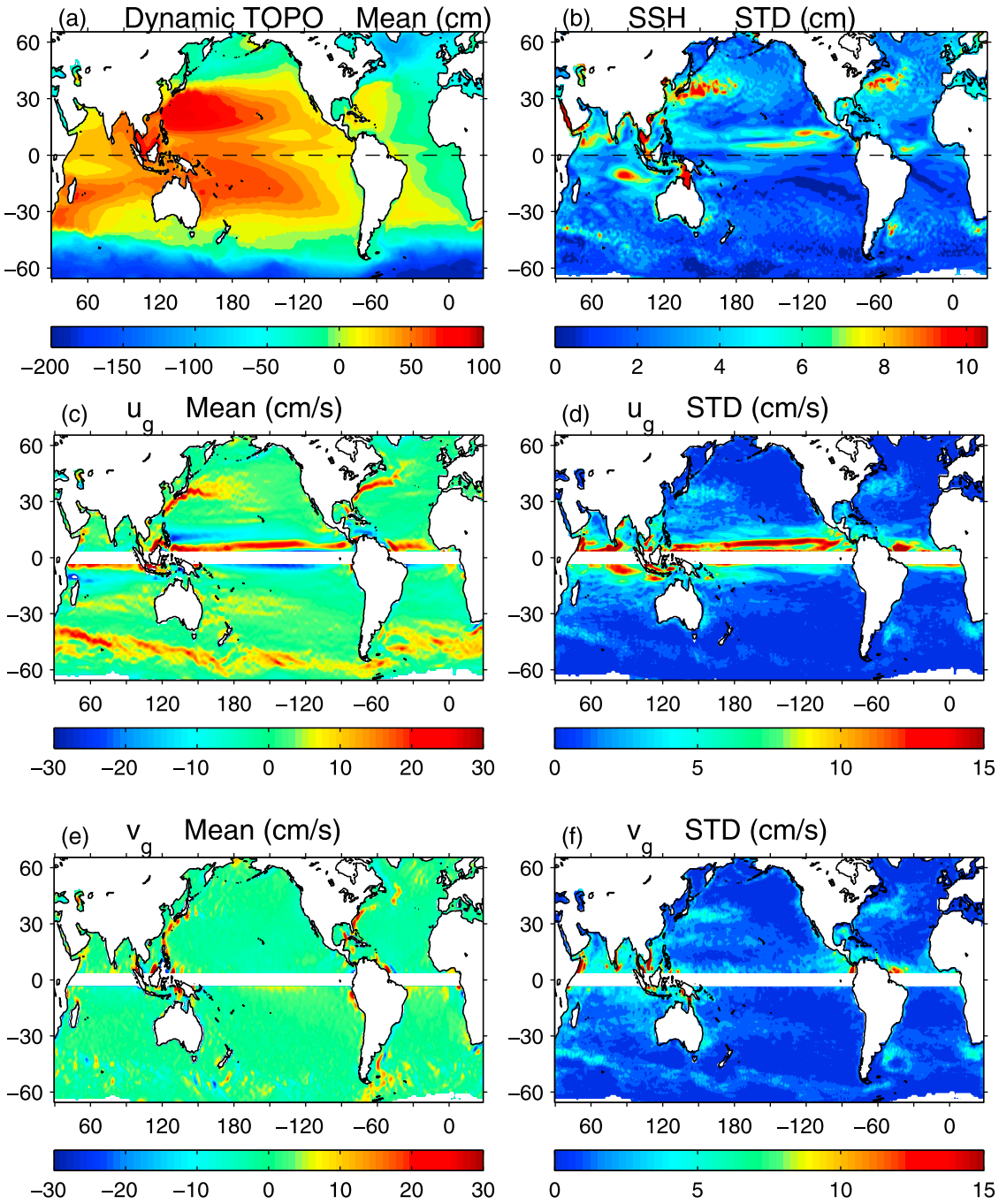

Figure 4. Annual mean and seasonal STD fields (a and b) for ocean surface topography, (c and d) for zonal geostrophic velocity (u_g), and (e and f) for meridional geostrophic velocity (v_g).

Pacific, the north tropical Atlantic, and the north Indian Ocean. Away from the tropical oceans, large seasonal variance in $\partial S/\partial y$ occurs mostly near the coasts.

2.3.3. Ekman and Geostrophic Currents

[28] The Ekman currents are computed in the same manner as by *Lagerloef et al.* [1999], in which the wind stressed upper ocean layer is considered to be a well-mixed slab with uniform velocity. Here the Ekman currents are obtained by scaling the Ekman transport in equation (2) with an effective depth. The effective depth is given as 32.5 m by *Lagerloef et al.* [1999] for the tropical Atlantic and is given as 26.5 ± 3 m by *Ralph and Niiler* [1999] for the tropical Pacific. In this study the effective depth is equivalent to the mixed layer depth if the latter is shallower than 30 m; otherwise it is set to 30 m. The mean pattern and STD of the Ekman and geostrophic currents are shown in Figures 3 and 4, respectively. Because the Coriolis parameter vanishes at the equator, the Ekman and geostrophic terms are masked out in the equatorial band within 3°S–3°N.

[29] The center of action in the mean pattern and seasonal STD of the zonal (u_{EK}) and meridional (v_{EK}) Ekman velocities (Figures 3a and 3c) is in the tropical oceans. The

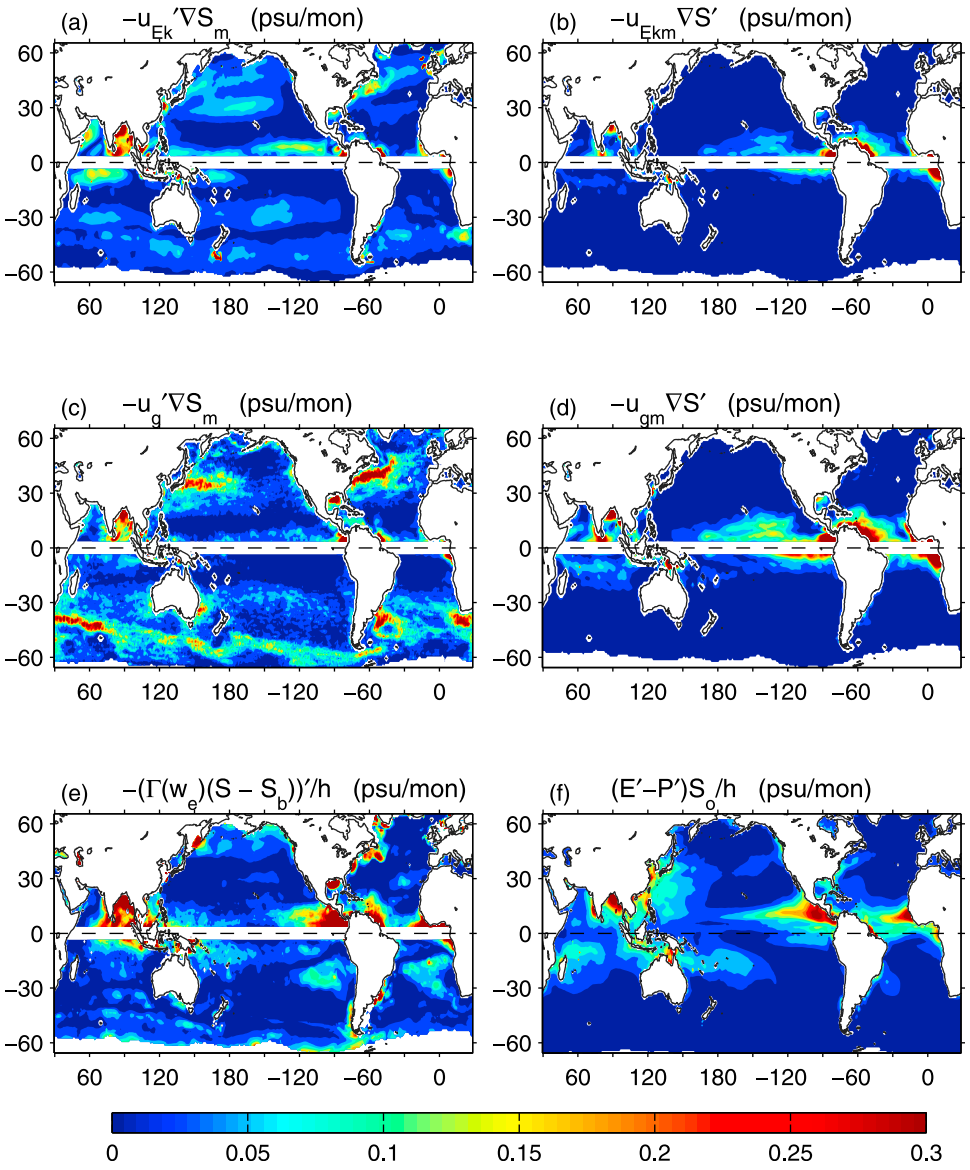

Figure 5. Seasonal STD fields in (a) anomalous Ekman advection ($\mathbf{U'_{EK}} \cdot \nabla\overline{S}$), (b) mean Ekman advection ($\overline{\mathbf{U}}_{\mathbf{EK}} \cdot \nabla S'$), (c) anomalous geostrophic advection ($\mathbf{U'_g} \cdot \nabla\overline{S}$), (d) mean geostrophic advection ($\overline{\mathbf{U}}_{\mathbf{g}} \cdot \nabla S'$), (e) anomalous vertical entrainment $(\Gamma(w_e)(S - S_b))'/\overline{h}$, and (f) anomalous E-P forcing $((E' - P')S_0)/\overline{h}$.

mean Ekman flows are predominantly northwestward in the north tropical Pacific and Atlantic Oceans, southeastward in the north Indian Ocean, and southwestward in all south tropical oceans. Mean v_{EK} is evidently stronger than mean u_{EK}. Nevertheless, seasonal variance of the two components has a similar magnitude, and both show marked variability in the tropical oceans (Figures 3b and 3d).

[30] The mean surface dynamic topography from *Niiler et al.* [2003] (Figure 4a) depicts the large-scale geostrophic circulation at the sea surface [*Maximenko et al.*, 2009]. From the derived mean zonal (u_g) and meridional (v_g) geostrophic components (Figures 4c and 4e), it is evident that over the global scale the zonal geostrophic component dominates over the meridional component, as the latter is noticeable only in a narrow neighborhood along the GS and KE. Prevailing features of u_g are found in the vicinity of strong ocean jets, including the WBCs (e.g., the GS and KE), the tropical zonal currents (e.g., the eastward North Equatorial Countercurrent (NECC), the westward North Equatorial Current (NEC), and the westward South Equatorial Current (SEC)), and the Antarctic circumpolar current (ACC). Despite the dominant mean global structure, STD of u_g are concentrated primarily in the tropical oceans associated with NECC. Outside of the tropical oceans, u_g has a weaker STD with amplitude similar to that of v_g although the latter shows no marked mean pattern.

[31] Putting Figures 3 and 4 together, it can be seen that the mean pattern and seasonal variance of the zonal velocity are dominated by the geostrophic component, and the contribution of the wind-driven zonal component is secondary and mostly in the tropical oceans. In sharp contrast, the mean pattern and seasonal variance of the meridional

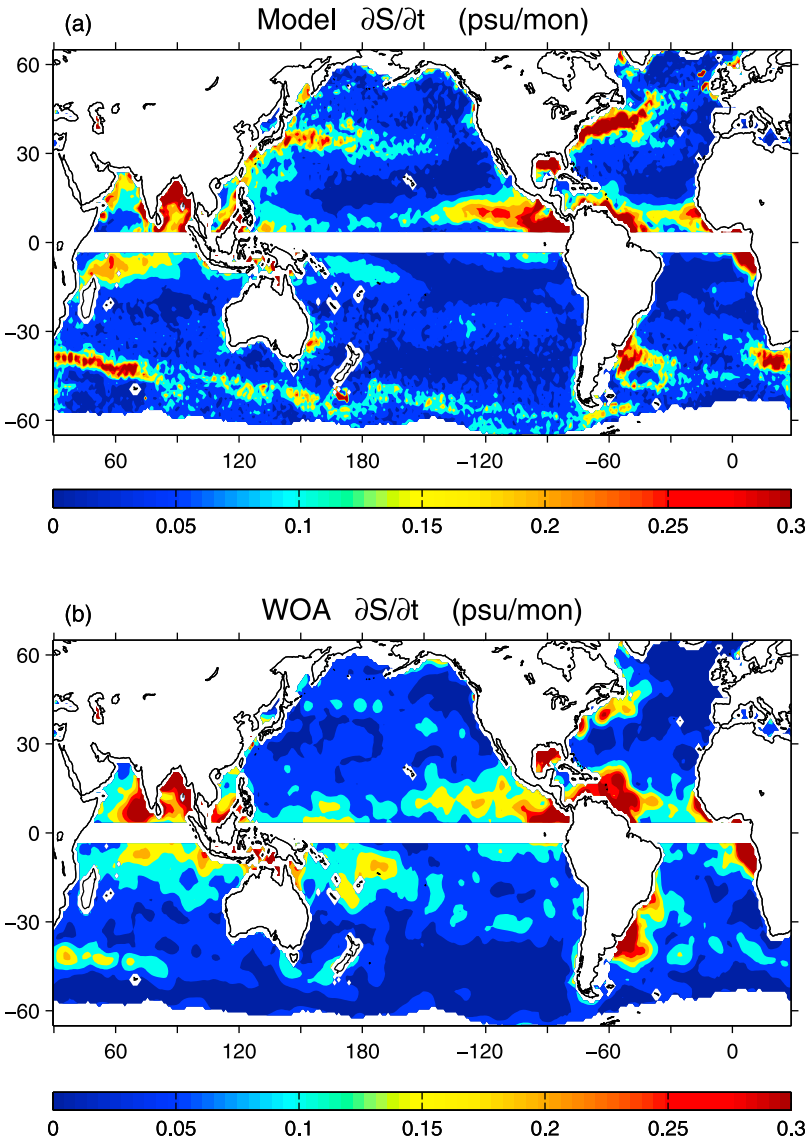

Figure 6. Seasonal STD of MLS tendency ($\partial S'/\partial t$) (a) computed from the right-hand-side of equation (4) and (b) derived from the WOA05 salinity climatology.

velocity are dominated by the Ekman component, with only minor contribution from geostrophy.

3. Contribution of the Leading Processes to Seasonal Variations of MLS

3.1. Seasonal Variances of the Processes in the MLS Budget Equation

[32] Using the data listed in section 2.2, the terms on the right-hand-side of equation (4) can be calculated. Seasonal STD of the major contributing terms are summarized in Figure 5. Salinity advections due to Ekman and geostrophic velocities are considered separately. The four horizontal advection terms in Figure 5 represent the advection of the mean MLS by seasonally varying Ekman ($-\boldsymbol{U}'_{EK} \cdot \nabla\overline{S}$, Figure 5a) and geostrophic velocities ($-\boldsymbol{U}'_g \cdot \nabla\overline{S}$, Figure 5c), and the advection of the MLS seasonal anomalies by mean Ekman ($-\overline{\boldsymbol{U}}_{EK} \cdot \nabla S'$, Figure 5b) and mean geostrophic velocities ($-\overline{\boldsymbol{U}}_g \cdot \nabla S'$, Figure 5d). Figure 5 also includes the salinity advection due to vertical entrainment/detrainment (Figure 5e), and the effective E-P forcing (Figure 5f). The diffusion term is not shown as we found that its contribution is negligible. In equation (4), this term is represented by a Laplacian horizontal diffusion with a coefficient κ set to 500 ms^{-2}. Different values were tested, and the results suggested that the value of κ does not affect the analysis of equation (4). Similar findings were also reported by *Dong et al.* [2009] in their budget analysis of the MLS in the south oceans.

[33] As is seen in Figures 5a–5f, prominent seasonal STD occur mostly in two major regimes: one is the tropical oceans north of the equator and the other is the vicinity of strong ocean currents in the extratropics. In the tropical oceans, the six terms all have substantial seasonal variances, and the largest STD come from the seasonal Ekman advection ($-\boldsymbol{U}'_{EK} \cdot \nabla\overline{S}$ Figure 5a), the vertical entrainment (Figure 5e), and E-P (Figure 5f). In the vicinity of strong ocean currents, STD of the seasonal geostrophic advection

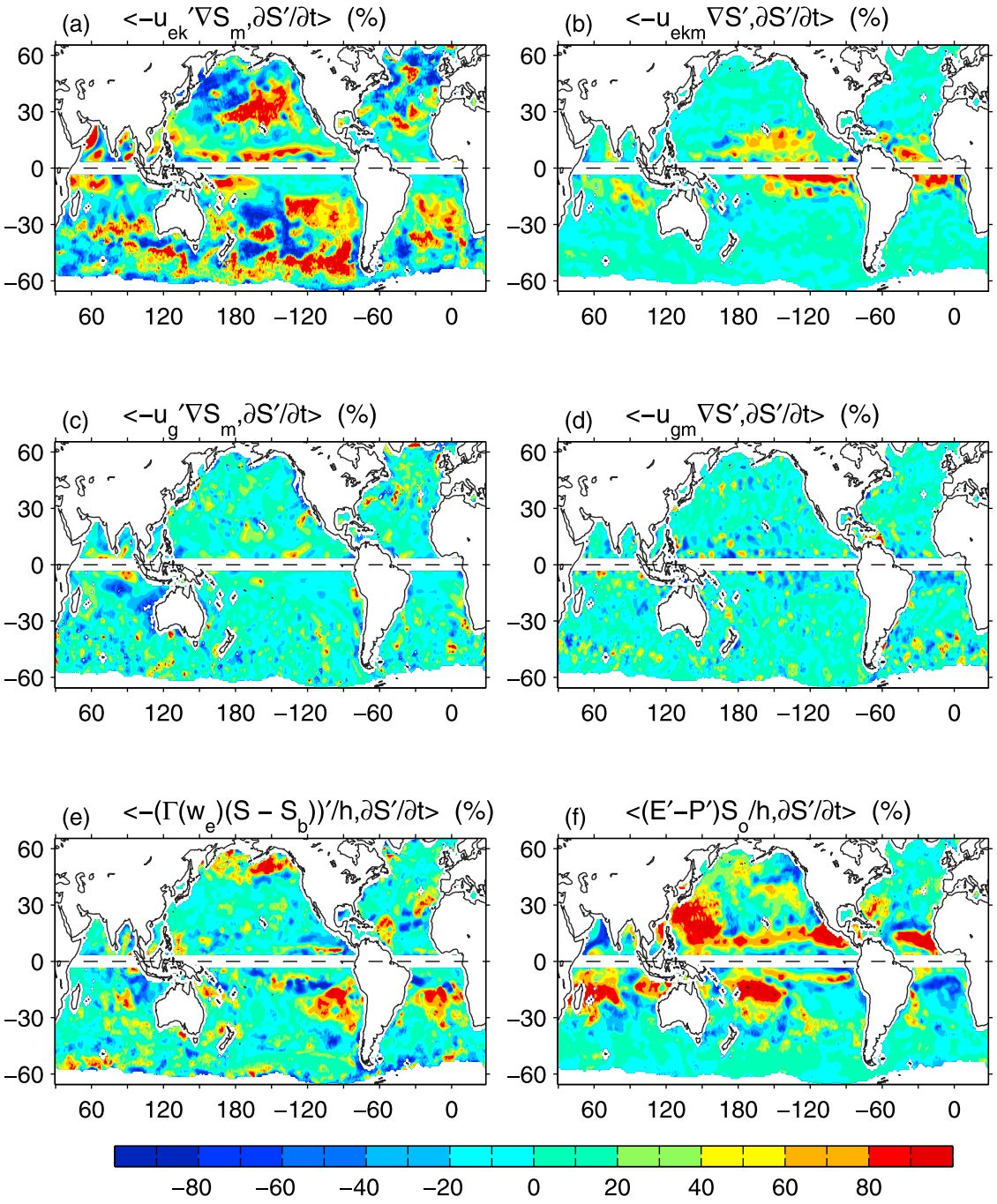

Figure 7. Normalized covariance between MLS tendency ($\partial S'/\partial t$) and the contributing process of (a) anomalous Ekman advection, (b) mean Ekman advection, (c) anomalous geostrophic advection, (d) mean geostrophic advection, (e) anomalous vertical entrainment, and (f) anomalous E-P forcing. The covariance for the diffusion term is not shown. The normalization denotes the scaling of the covariance by the sum of all the covariance matrices (a total of 7 covariances including the diffusion term).

($-\boldsymbol{U}_g' \cdot \nabla\overline{S}$, Figure 5c) dominate, followed by the STD of the seasonal Ekman advection ($-\boldsymbol{U}_{EK}' \cdot \nabla\overline{S}$, Figure 5a). STD of the mean Ekman and geostrophic advection (Figures 5b and 5d) are sufficiently large in the tropical oceans, but diminish quickly away from the tropics as horizontal salinity gradients in the extratropics (Figures 2b and 2d) change little on seasonal timescales.

3.2. The Ratio $\partial S'/\partial t$ Determined From WOA and From the Model-Based Analysis

[34] By integrating the terms on the right-hand-side of equation (4) over the 12 months, we can obtain the rate of the monthly change of MLS, i.e., $\partial S'/\partial t$. On the other hand, $\partial S'/\partial t$ can also be derived directly from the monthly MLS constructed from the WOA climatology. The seasonal STD

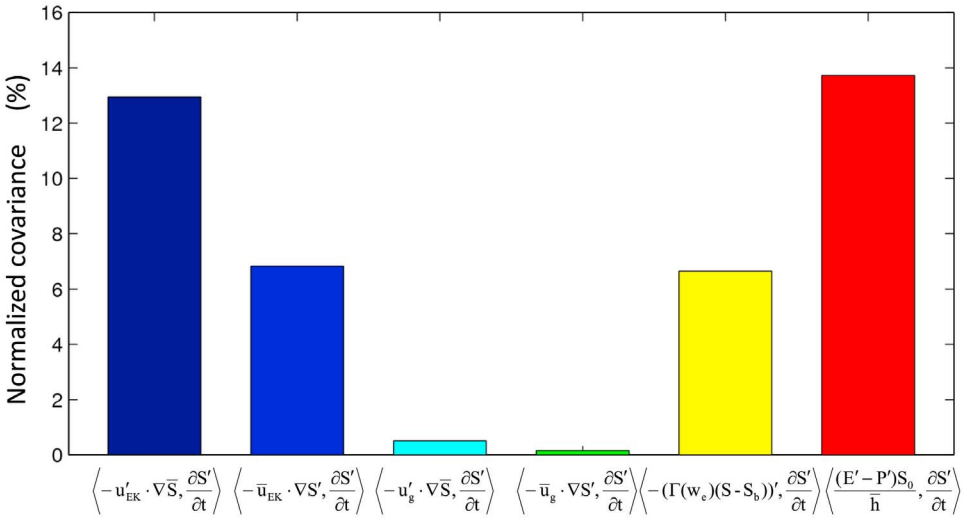

Figure 8. Bar plot of the percentage contribution of each contributing process to MLS tendency ($\partial S'/\partial t$) over the global ocean.

of $\partial S'/\partial t$ computed from the two approaches are shown in Figures 6a and 6b, respectively, displaying a remarkably good agreement in the overall structures. Both show that major seasonal variance of $\partial S'/\partial t$ occurs primarily in two regimes over the global oceans: the tropical oceans and the vicinity of the strong ocean currents in the extratropical oceans. Both also show that seasonal variance is insignificant or weak in the northern and southern subtropical oceans and at high northern latitudes. The broad consistency of the two patterns indicates that the first-order MLS balance based on equation (4) is resolved reasonably well by the satellite-derived data sets.

[35] Nevertheless, the two STD patterns do have differences in some detailed structures. For instance, the substantial seasonal variability of $\partial S'/\partial t$ along the KE that is seen in the model-based analysis is not featured in the WOA-based estimation. Similarly, the variability of $\partial S'/\partial t$ associated with the ACC is also not captured by the WOA-based estimation. The WOA climatology was constructed from inhomogeneous instrumentation and limited spatial coverage. The lack of seasonal variance of $\partial S'/\partial t$ in the vicinity of strong ocean currents may be related to the poor salinity samplings in these regions.

3.3. Covariance Analysis Between the Contributing Processes and $\partial S'/\partial t$

[36] The modeled pattern of seasonal variations in $\partial S'/\partial t$ (Figure 6a) represents the sum of the contributions from all the processes on the right-hand-side of equation (4). To examine the relative importance of each process, a covariance analysis is performed by pairing each process with the WOA-based $\partial S'/\partial t$. The covariance of $\partial S'/\partial t$ with the anomaly of a particular process, χ'_i, is denoted $\langle \chi'_i, \partial S'/\partial t\rangle$, and the normalization by the total combined covariance of all the terms with $\partial S'/\partial t$ can be expressed as

$$\frac{\left\langle \chi_i', \frac{\partial S'}{\partial t}\right\rangle}{\sqrt{\sum_{i=1}^{7}\left(\left\langle \chi_i', \frac{\partial S'}{\partial t}\right\rangle\right)^2}} \tag{5}$$

Figures 7a–7f show the normalized covariance for each of the six processes (diffusion is not included). Positive values denote that the process tends to enhance the MLS tendency, while negative values denote that the process tends to reduce the MLS tendency. Among all the terms, the seasonal Ekman advection (Figure 7a) and E-P (Figure 7f) are the dominant contributors, followed by the mean Ekman advection (Figure 7b) and vertical entrainment (Figure 7e). Contributions of the mean and seasonal geostrophic advection (Figures 7c and 7d) are generally noisy, although a 1-2-1 smoother has been applied to both fields. It is not clear whether the lack of covariability between $\partial S'/\partial t$ and the geostrophic advection is due to the lack of adequate salinity sampling in the WOA salinity climatology.

[37] The seasonal Ekman advection (Figure 7a) contributes positively to the seasonal variance of $\partial S'/\partial t$ in two major areas, the tropical Pacific and Indian Oceans and the subtropical oceans. The latter regions include the subtropical northern and southern Pacific and the southern Atlantic. An examination of the seasonal Ekman velocity (Figure 3) and the mean salinity gradient fields (Figure 2) suggests that the spatial pattern of the covariance $\langle -\boldsymbol{U}'_{EK}\cdot\nabla\overline{S}, \partial S'/\partial t\rangle$ is due largely to the mean meridional salinity gradient. In the tropical Pacific and Atlantic oceans, the contribution from the mean Ekman advection is also considerable (>40%) (Figure 7b). Nevertheless, the effects of the mean and seasonal Ekman advections on $\partial S'/\partial t$ do not overlap. For instance, the seasonal Ekman effect is confined along a narrow zonal band located primarily north of the equator, while the mean Ekman advection affects the areas on the two sides of this band. The regional difference between the two Ekman effects is attributed more to the structural difference in the mean and seasonal meridional Ekman velocities in the tropical ocean (Figures 3c and 3d).

[38] Prominent contribution (>80%) by the entrainment process to the MLS tendency is observed in the northern North Pacific (45°N poleward) and also in the subtropical southeastern Pacific and the subtropical north and south Atlantic. Interestingly, these areas of large positive contribution by the entrainment overlap with the areas of

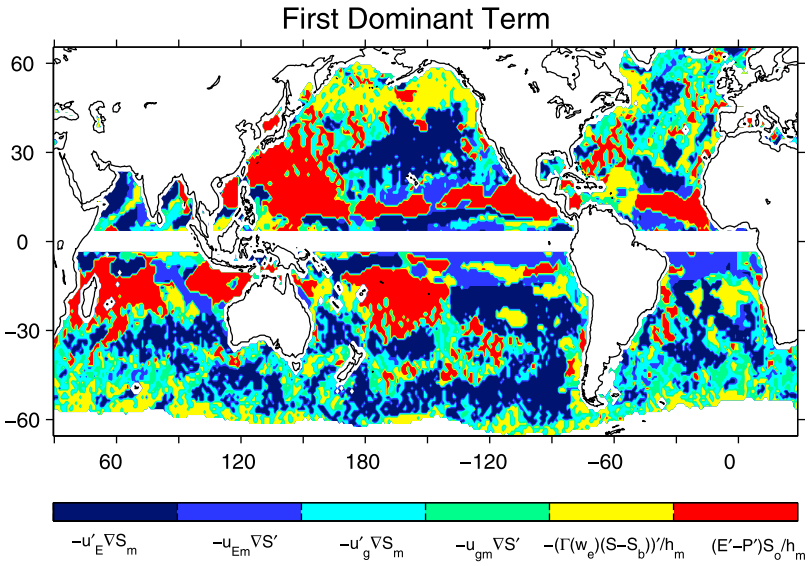

Figure 9. Map of the leading dominant term over the global ocean.

negative contribution by *E-P*, suggesting that in these regions the two processes have a compensating effect on the MLS surface budget, with the entrainment process being slightly dominant.

[39] The *E-P* effect on the MLS tendency is located primarily in the tropical convergence zones (ITCZ and SPCZ) and the western North Pacific (Figure 7f). Compared to the seasonal STD pattern of *E-P* (Figure 1f), it is apparent that the regions where *E-P* has a large contribution to $\partial S'/\partial t$ are the regions where seasonal variance of *E-P* is most prominent. This suggests that the magnitude of *E-P* variability might be a useful measure for understanding the role of *E-P* in seasonal variability of $\partial S'/\partial t$.

[40] Partition of the six leading processes to global seasonal variability of $\partial S'/\partial t$ is shown in Figure 8. The *E-P* forcing and seasonal Ekman advection are the two dominant terms, with the former accounting for 13.7% of seasonal variance of the MLS tendency and the latter 12.9%. The mean Ekman advection and the entrainment process are of secondary importance, and both have roughly the same amount of contribution (~7%) to global $\partial S'/\partial t$. By comparison, neither the mean nor the seasonal geostrophic advections has substantial covariability with the MLS tendency, as each contributes less than 1% globally. When summing up the contributions from all the six processes, the model-based analysis explains about 40% of global variability of the observed MLS tendency on seasonal timescales. It is not surprising that the sum of the six covariances cannot fully account for the observed total seasonal variance of the MLS. Leading cause of the underrepresentation includes the use of a lower-order MLS budget equation that does not resolve all the processes contributing to the MLS (such as the effects of the frontal mixing and shear instabilities), the treatment that the six contributing processes are weakly correlated and thus the covariances between them are not considered, the inhomogeneous sampling in the WOA climatology that may cause low correlation between modeled processes and observed salinity variability, and the uncertainties in satellite-derived data sets.

4. Mapping the Global Relationship Between *E-P* and $\partial S'/\partial t$

4.1. The Global Pattern of the Leading Dominant Process

[41] Figure 7 indicates that the seasonal variability of $\partial S'/\partial t$ in different regions is dominated by different processes. Accordingly, the relative importance of the six processes can be ranked in terms of the magnitude of the covariance with respect to $\partial S'/\partial t$ at each grid point. By plotting the rank order over the global domain, we can obtain a big-picture perspective of the global influence of each process, particularly, the influence of *E-P* versus that of the Ekman advection. The first dominant term is shown in Figure 9, which appears to be a good summary of Figures 7a–7f, with the following five features most noteworthy.

[42] The first feature is the predominance of *E-P* in the tropical convergence zones (i.e., the areas marked by red in Figure 9). An examination of Figure 7f indicates that the *E-P* dominant regime consists of the regions where the magnitude of the normalized covariance between *E-P* and $\partial S'/\partial t$ exceeds 60%. Many studies have reported that the heavy precipitation associated with deep convection is a primary forcing for seasonal variability of the MLS [e.g., *Delcroix et al.*, 1996; *Boyer and Levitus*, 2002; *Bingham et al.*, 2010], the outlined pattern of the *E-P* dominance is a fair synthesis of these studies. One interesting finding of this study is that the precipitation zones are not the only component in the *E-P* dominant regime. The regime includes also a substantial portion of the western North Pacific and a limited area in the western North Atlantic, both of which are subject to the influence of *E* (Figures 1b and 1f).

[43] The second feature is the large-scale dominance of the seasonal Ekman advection, particularly in the north and south subtropical Pacific (i.e., the areas marked by dark blue

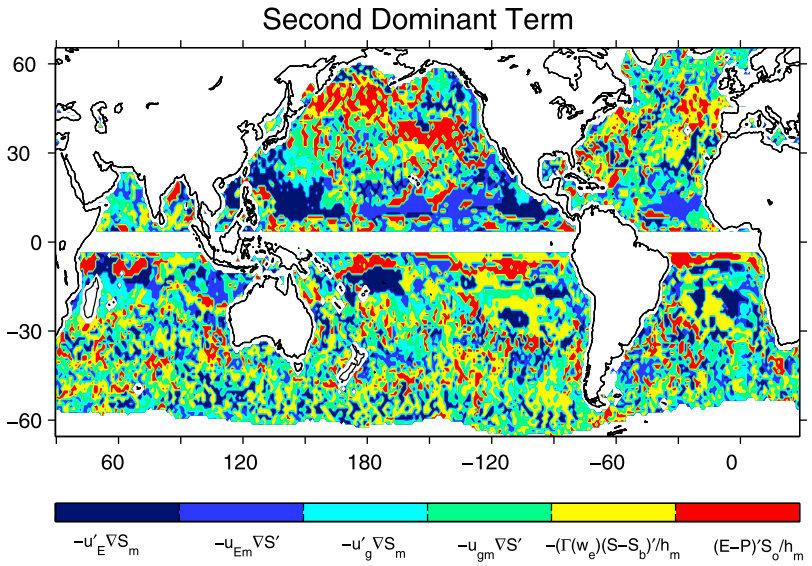

Figure 10. Map of the second dominant term over the global ocean.

in Figure 9). The influential role of the Ekman advection depicted here is in good agreement with the findings of numerous previous studies [e.g., *Delcroix and Hénin*, 1991; *Lukas*, 2001; *Johnson et al.*, 2002; *Rao and Sivakumar*, 2003; *Reverdin et al.*, 2007; *Foltz and McPhaden*, 2008; *Ren and Riser*, 2009; *Bingham et al.*, 2010]. The pattern here supports the argument that salinity anomalies tend to be more prone to the influence of ocean advection/mixing processes, particularly in mid latitudes [*Spall*, 1993; *Hall and Manabe*, 1997; *Mignot and Frankignoul*, 2003, 2004].

[44] The third feature in Figure 9 (i.e., the areas marked by yellow) delineates the importance of the entrainment process for seasonal salinity variability in the North Pacific (30–60°N) and at high southern latitudes (50°S poleward). *Ren and Riser* [2009] analyzed the seasonal MLS budget in a subregion [45–50°N, 155–140°W] of the northeastern Pacific. They found that in fall and winter when the mixed layer depth increases and the entrainment velocity is largest, entrainment plays an important role in bringing up the salty subsurface water to balance the surface freshening effect. *Dong et al.* [2009] did a seasonal MLS budget analysis for the south ocean (35–65°S) and had a similar finding, that is, entrainment is the essential term to balance the surface freshening anomalies induced by *E-P* and by the horizontal advection. Apparently, Figure 9 is a sensible depiction of the role of the entrainment in the seasonal change of $\partial S'/\partial t$ at higher latitudes.

[45] The fourth feature is the confinement of the mean Ekman advection in the tropical oceans in the vicinity of the *E-P* dominant regime. It is known that *E-P* generates salinity anomalies but does not dampen them due to the lack of a feedback mechanism. The pattern in Figure 9 implies that the advection by the mean Ekman currents serves as a key agent in carrying the salinity anomalies away from the generation sites. Previous studies of the surface salinity budget in the tropical oceans have suggested that a substantial portion of the *E-P* input can be balanced by the ocean advection in a thin surface layer [*Delcroix and Hénin*, 1991; *Johnson et al.*, 2002] and that *E-P* can explain the phase, but not the magnitude, of the salinity change in the region [*Delcroix et al.*, 1996].

[46] The last but not the least feature is the difference between Figures 8 and 9 in projecting the role of the geostrophic advections in global salinity variability. Figure 8 shows that the advection by geostrophy has limited contribution. However, Figure 9 shows that a substantial amount of the MLS tendency in the extratropical Atlantic Ocean is governed by the salt transport due to geostrophy. The discrepancy between Figures 8 and 9 may be due to the noisy grid-size structures in the covariance between the geostrophic advection and $\partial S'/\partial t$ (Figures 7c and 7d), as there might be a significant cancellation when summed up all the covariances over the global oceans.

4.2. Pattern of the Second Leading Process

[47] The global pattern of the second dominant process for seasonal salinity variability (Figure 10) provides additional evidence of the prevalence of the Ekman advection. In the same 10–20° latitude bands where *E-P* shows the primary dominance (the area marked by red in Figure 9), the Ekman advection by mean and seasonally varying flows is the second important process in the local MLS budget, which supports the findings of previous studies [*Delcroix and Hénin*, 1991; *Johnson et al.*, 2002]. Except for the tropical oceans where the influence of the Ekman terms is well structured, the overall pattern of the second dominance process is generally noisy. Nevertheless, we can still derive some indication that *E-P* is a leading secondary process in the North Pacific and Atlantic oceans in the latitude bands of 30–60°N, and the influence of entrainment is evident over most of the extratopical oceans.

4.3. Relative Role of *E* and *P* in the *E-P* Dominant Regime

[48] The *E-P* dominant regime includes both the regions of excessive precipitation (i.e., tropical convergence zones)

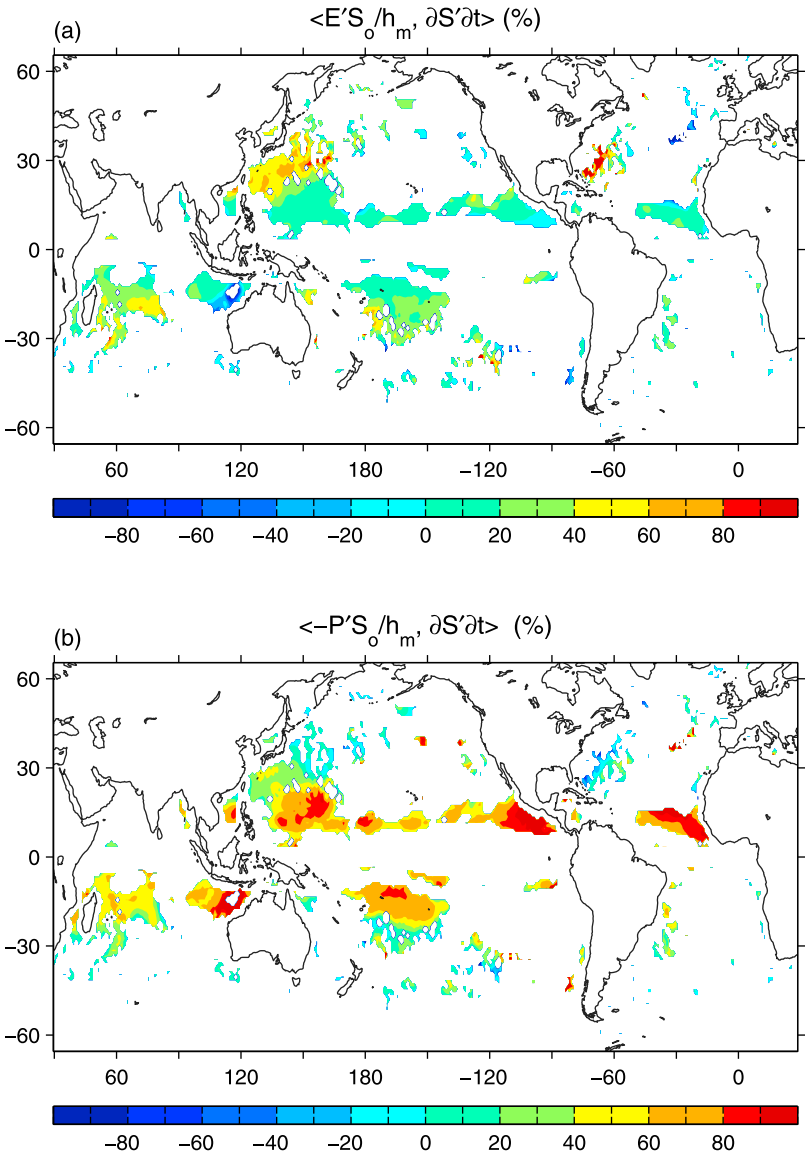

Figure 11. Normalized covariance (a) between $\partial S'/\partial t$ and E' and (b) between $\partial S'/\partial t$ and P' in the E-P dominant regime.

and the regions of excessive evaporation (i.e., the western North Pacific). Given that the MLS tendency responds to the net E-P forcing, it would be interesting to know the contribution of the E component in the P-dominating regions and likewise, the contribution of the P component in the E-dominating regions. Hence, we computed the normalized covariance for both the E and $\partial S'/\partial t$ pair and the P and $\partial S'/\partial t$ pair and compared them in Figures 11a and 11b. It can be seen that the E-driven freshwater forcing in the western North Pacific explains slightly more than 40% of seasonal variability of the local MLS. *Bingham et al.* [2010] applied a harmonic analysis to a multisource salinity database and found similar results. Specifically, they showed that the change in MLS is balanced mostly by the local E and entrainment while the horizontal advections play relatively minor roles. Significant covariance (>80%) between E and $\partial S'/\partial t$ also appears in a limited area in the western North Atlantic. However, the local P has a generally negative correlation with $\partial S'/\partial t$, which tends to cancel out the effect of E and causes the combined E-P forcing to be less commanding (Figure 7f).

[49] Overall, E is more influential for salinity variability in the extratropical regions and explains about 40% of seasonal variance of local salinity, while P is a leading forcing in the tropical convergence zones and contributes to more than 60% of seasonal variances of regional salinity. When E and P are combined, covariability between the net freshwater forcing and $\partial S'/\partial t$ increases over most of the E-P dominant regime and E-P can accounts for 40–70% of the seasonal variability of $\partial S'/\partial t$. It should be noted that the covariance analysis neglected the covariance between the contributing processes themselves; hence the percentage of MLS variance attributed to E and P could be overestimated.

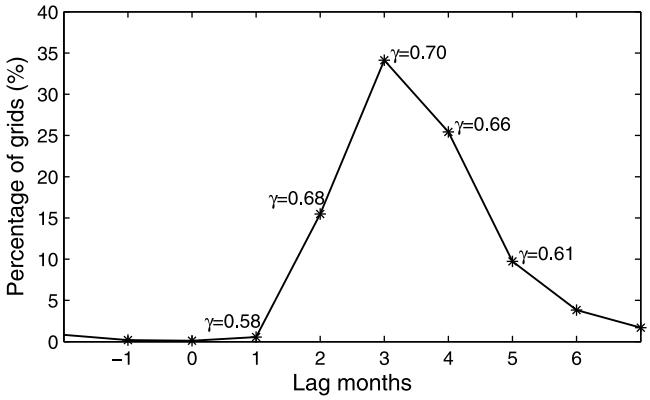

Figure 12. Percentage of the area versus the response time of MLS tendency to seasonal change of the *E-P* forcing calculated from cross-correlation for the *E-P* dominant regime. The correlation coefficients (denoted by γ) averaged over the area are shown for phase lag (i.e., MLS lags *E-P*) at 0, 1, 2, and 3 months.

4.4. Lagged Correlation Between the MLS and *E-P* in the *E-P* Dominant Regime

[50] The response of MLS anomalies to *E-P* is at 90 degrees phase lag, or a quarter of cycle. The correlations between the MLS and *E-P* seasonal anomalies in the *E-P* dominant regime were computed with both time leads (from −6 to −1 month) and time lags (from 0 to 6 months). Figure 12 shows the averaged area distribution of the correlations between the two variables for the MLS phase lags from −2 to 7 months. The correlation peaks when the MLS lags *E-P* by 3 month, and this occurs over 35% of the *E-P* dominant regime. For the annual cycle, a quart of cycle is 3 months, which explains the occurrence of the maximum correlation at this lag. Overall, the optimal response of the MLS anomalies to *E-P* occurs at a lag time between 2 and 4 months. At these phase lags, the correlation coefficients range from 0.66 to 0.70, all at the 90% confidence level. Since *E-P* is not the sole mechanism for the seasonal change of the MLS, the significant correlations at lags other than the anticipated 3 months underline the influence of other processes (such as Ekman advection) on the MLS.

5. Summary and Conclusions

[51] The MLS and *E-P* are related through complex upper ocean dynamics. One issue central to the concept of using the oceans as a rain gauge for the marine branch of the global water cycle is how closely these two variables are related over the global oceans. This study attempted to address this issue by using covariance analysis to quantify relative contribution of the key balance processes in the seasonal MLS budget. The analysis was based on satellite-derived data sets from several sources including GPCP precipitation, OAFlux evaporation and wind stress, AVISO SSH, the mean dynamic ocean topography from *Maximenko et al.* [2009], and the salinity climatology from the WOA05. A lower-order dynamics of the MLS budget was derived so that the key balance terms can all be computed from existing data sets. These terms include *E-P*, the horizontal salt advection by seasonal and mean Ekman velocities, the horizontal salt advection by seasonal and mean geostrophic velocities, vertical entrainment, and horizontal diffusion. The diffusion term is found to be small and not included in the plots.

[52] One major result is a global map that outlines the dominance regions of *E-P* and oceanic processes (Figure 9). There are two areas where *E-P* shows a predominant role in seasonal variability of MLS. One is the tropical convergence zones that are subject to high precipitation, and the other is the western North Pacific and a limited area in the western North Atlantic that are subject to high evaporation. Within the *E-P* dominant regime, *E-P* accounts for 40–70% MLS variance with peak correlations occurring at 2–4 month lead time (Figure 12). Evaporation alone accounts for about 23% of the MLS variance on average, with the maximum effect (>40%) over the western North Pacific and a limited area in the western North Atlantic (Figure 10). By contrast, precipitation alone contributes to more than 60% of the MLS variance in the tropical convergence zones. It should be noted that the covariance analysis neglected the covariance between the contributing processes themselves; hence the percentage of MLS variance attributed to *E* or *P* could be overestimated.

[53] The map also shows a large-scale dominance of the salt advection by the Ekman transport, with mean Ekman advection controlling the tropical oceans and seasonally varying Ekman components controlling the extratropical oceans. Vertical entrainment has a major role in seasonal change of the MLS in the North Pacific (30–60°N) and at high southern latitudes (50°S poleward). By comparison, the geostrophic advection has only a slight contribution to the MLS in a few areas of the extratropical Atlantic Ocean. On the global scale, the total contribution of the geostrophic advection is small (Figure 8). It appears that the lack of the salinity variability in the vicinity of strong ocean currents in WOA05 is the main reason of the limited contribution of the geostrophy to global salinity variability. It is not clear whether the issue is related to spatial/temporal undersampling of salinity in the frontal regions.

[54] The terms on the right-hand-side of equation (4), when summed up together, can explain only about 40% of seasonal variance of the MLS over the global oceans (Figure 8), indicating that there is substantial imbalance in the present MLS budget analysis that is based on a lower-order salinity dynamics. The imbalance can be attributed to uncertainties in both data and model. For instance, the lower-order MLS budget equation does not resolve all the processes contributing to the MLS (such as the effects of the frontal mixing and shear instabilities), the treatment that the six contributing processes are uncorrelated neglects the covariances between these contributing processes, the inhomogeneous sampling in the WOA climatology may cause low correlation between modeled processes and observed salinity variability, and the uncertainties in satellite-derived data sets may also affect the correlation between the modeled and the observed change in the MLS. One question being raised by a reviewer is the sensitivity of the derived global *E-P* dominant regime to the *E-P* products, in particular whether different *P* products would cause a change of the pattern as *P* is a major contributor. Our experience shows that the effects of the uncertainties in *E* and *P* estimates are timescale dependent. Most products deviate from each other on the mean structure as well

as the long-term trend and variability, but they agree well on seasonal timescales [*Yin et al.*, 2004; *Yu et al.*, 2007]. To test the robustness of Figure 9, we replaced GPCP with the CPC merged Analysis of precipitation (CMAP) [*Xie et al.*, 2007] and re-conducted the covariance analysis. Regardless of the widely documented difference in the mean pattern of the two precipitation data sets [e.g., *Yin et al.*, 2004], we found that the resulting map of the global *E-P* dominance is almost identical to Figure 9 because the seasonal variance of CMAP is very similar to GPCP (not shown).

[55] In summary, Figure 9 is a feasible first-order depiction of the global dominance of *E-P* and ocean advection on seasonal MLS variability. It shows that there exists an *E-P* dominant regime in the tropical oceans and that in this regime near-surface salinity could be used as a window to build the understanding of the global water cycle variability. Nevertheless, the study is based on a lower-order MLS dynamics that considers only key balance terms resolvable by satellite-derived data sets and the WOA salinity climatology. The validity of this big-picture perspective needs to be fully evaluated with the soon-to-be available satellite salinity measurements and/or the salinity-assimilated ocean general circulation model (OGCM) that implements a full MLS dynamics. Some data-assimilated OGCMs such as the ECCO ocean state estimator [*Wunsch et al.*, 2009] can produce an estimate of the surface net freshwater flux. At present, the surface freshwater fluxes provided by data-assimilated ocean models differ substantially from each other [*Yu*, 2006] and from the satellite-derived *E-P* products such as the one used in this study. It is anticipated that the surface salinity from space combined with the provision of regular surface and sub-surface salinity profiles from in situ observing systems will provide a better data constraint for OGCMs to improve the model representation of the global freshwater balance and to improve the estimation of the surface heat and freshwater fluxes. It is anticipated that the satellite salinity mission will energize the research activities on the global water cycle and encourage new innovative approaches to reconcile the *E-P* estimates derived from satellites with those from data-assimilated OGCMs and to reconcile the observed salinity changes [e.g., *Wang et al.*, 2010] with our understanding of the change in the global water cycle.

[56] **Acknowledgments.** The study was supported by the NASA Remote Sensing Science for Carbon and Climate program under grant NNX07AF97G and by the NSF Physical Oceanography program under grant OCE-0647949. Support from the NOAA Office of Climate Observation (OCO) and NASA Ocean Vector Wind Science Team (OVWST) in developing OAFlux evaporation and surface wind stress used in the study are gratefully acknowledged. The author thanks two anonymous reviewers for constructive comments which led to improved presentation of the paper. Monthly SSH climatology is downloaded from ftp://ftp.aviso.oceanobs.com/, the mean dynamic ocean topography from http://apdrc.soest.hawaii.edu/projects/DOT/, GPCP monthly precipitation analysis from http://www1.ncdc.noaa.gov/pub/data/gpcp/gpcp-v2.1/, OAFlux evaporation and wind analyses from http://oaflux.whoi.edu, and the WOA climatology from http://www.nodc.noaa.gov/OC5/WOD05/pr_wod05.html.

References

Adler, R. F., et al. (2003), The Version-2 Global Precipitation Climatology Project (GPCP) monthly precipitation analysis (1979–present), *J. Hydrometeorol.*, *4*, 1147–1167, doi:10.1175/1525-7541(2003)004<1147:TVGPCP>2.0.CO;2.

Andersson, A., C. Klepp, K. Fennig, S. Bakan, H. Graßl, and J. Schulz (2011), Evaluation of HOAPS-3 ocean surface freshwater flux components, *J. Appl. Meteorol. Climatol.*, *50*, 379–398, doi:10.1175/2010JAMC2341.1.

Antonov, J. I., R. A. Locarnini, T. P. Boyer, A. V. Mishonov, and H. E. Garcia (2006), *World Ocean Atlas 2005*, vol. 2, *Salinity*, NOAA Atlas NESDIS, vol. 62, edited by S. Levitus, 182 pp., NOAA, Silver Spring, Md.

AVISO (2009), SSALTO/DUACS user handbook: (M)SLA and (M)ADT near-real time and delayed time products, *Ref. CLS-DOS-NT-06.034*, 51 pp., AVISO Altimetry, Ramonville-Saint-Agne, France.

Baumgartner, A., and E. Reichel (1975), *The World Water Balance*, 179 pp., Elsevier, New York.

Berger, M., et al. (2002), Measuring ocean salinity with ESA's SMOS Mission, *ESA Bull.*, *111*, 113–121.

Bingham, F. M., G. R. Foltz, and M. J. McPhaden (2010), Seasonal cycles of surface layer salinity in the Pacific Ocean, *Ocean Sci.*, *6*, 775–787, doi:10.5194/os-6-775-2010.

Boyer, T. P., and S. Levitus (2002), Harmonic analysis of climatological sea surface salinity, *J. Geophys. Res.*, *107*(C12), 8006, doi:10.1029/2001JC000829.

Boyer, T. P., S. Levitus, J. I. Antonov, R. A. Locarnini, and H. E. Garcia (2005), Linear trends in salinity for the World Ocean, 1955–1998, *Geophys. Res. Lett.*, *32*, L01604, doi:10.1029/2004GL021791.

Chang, C.-P., P. A. Harr, J. McBride, and H. H. Hsu (2004), Maritime Continent monsoon: Annual cycle and boreal winter variability, in *East Asian Monsoon*, *Ser. Meteorol. East Asia*, vol. 2, edited by C.-P. Chang, pp. 107–150, World Sci., Singapore.

Cravatte, S., T. Delcoix, D. Zhang, M. McPhaden, and J. LeLoup (2009), Observed freshening and warming of the western Pacific Warm Pool, *Clim. Dyn.*, *33*, 565–589, doi:10.1007/s00382-009-0526-7.

Cronin, M. F., and M. J. McPhaden (1998), Upper ocean salinity balance in the western equatorial Pacific, *J. Geophys. Res.*, *103*(C12), 27,567–27,587, doi:10.1029/98JC02605.

Curry, R., R. Dickson, and I. Yashayaev (2003), Ocean evidence of a change in the fresh water balance of the Atlantic over the past four decades, *Nature*, *426*, 826–829, doi:10.1038/nature02206.

de Boyer Montégut, C., G. Madec, A. S. Fischer, A. Lazar, and D. Iudicone (2004), Mixed layer depth over the global ocean: An examination of profile data and a profile-based climatology, *J. Geophys. Res.*, *109*, C12003, doi:10.1029/2004JC002378.

Delcroix, T., and C. Hénin (1991), Seasonal and interannual variations of sea-surface salinity in the tropical Pacific ocean, *J. Geophys. Res.*, *96*, 22,135–22,150, doi:10.1029/91JC02124.

Delcroix, T., C. Henin, V. Porte, and P. Arkin (1996), Precipitation and sea surface salinity in the tropical Pacific, *Deep Sea Res.*, *43*, 1123–1141, doi:10.1016/0967-0637(96)00048-9.

Dessier, A., and J. R. Donguy (1994), The sea-surface salinity in the tropical Atlantic between 10°S and 30°N—Seasonal and interannual variations (1977–1989), *Deep Sea Res., Part I*, *41*, 81–100, doi:10.1016/0967-0637(94)90027-2.

Dickson, R. R., J. Meincke, S.-A. Malmberg, and A. J. Lee (1988), The "Great Salinity Anomaly" in the North Atlantic, 1968–1982, *Prog. Oceanogr.*, *20*, 103–151, doi:10.1016/0079-6611(88)90049-3.

Dong, S., S. L. Garzoli, and M. Baringer (2009), An assessment of the seasonal mixed layer salinity budget in the Southern Ocean, *J. Geophys. Res.*, *114*, C12001, doi:10.1029/2008JC005258.

Donguy, J.-R., and G. Meyers (1996), Seasonal variations of sea-surface salinity and temperature in the tropical Indian Ocean, *Deep Sea Res., Part I*, *43*, 117–138, doi:10.1016/0967-0637(96)00009-X.

Elliott, G. W. (1974), Precipitation signatures in sea-surface-layer conditions during BOMEX, *J. Phys. Oceanogr.*, *4*, 498–501, doi:10.1175/1520-0485(1974)004<0498:PSISSL>2.0.CO;2.

Fairall, C. W., E. F. Bradley, J. E. Hare, A. A. Grachev, and J. B. Edson (2003), Bilk parameterization of air-sea fluxes: Updates and verification for the COARE algorithm, *J. Clim.*, *16*(4), 571–591, doi:10.1175/1520-0442(2003)016<0571:BPOASF>2.0.CO;2.

Foltz, G. R., and M. J. McPhaden (2008), Seasonal mixed layer salinity balance of the tropical North Atlantic Ocean, *J. Geophys. Res.*, *113*, C02013, doi:10.1029/2007JC004178.

Frankignoul, C. (1985), Sea surface temperature anomalies, planetary waves and air–sea feedback in the middle latitudes, *Rev. Geophys.*, *23*, 357–390, doi:10.1029/RG023i004p00357.

Gruber, A., and V. Levizzani (2008), Assessment of global precipitation products, *Tech. Rep. WRCP-128, WMO/TD 1430*, 55 pp., World Clim. Res. Program, Geneva.

Hall, A., and S. Manabe (1997), Can local, linear stochastic theory explain sea surface temperature and salinity variability?, *Clim. Dyn.*, *13*, 167–180, doi:10.1007/s003820050158.

Johnson, E. S., G. S. E. Lagerloef, J. T. Gunn, and F. Bonjean (2002), Surface salinity advection in the tropical oceans compared with atmospheric freshwater forcing: A trial balance, *J. Geophys. Res.*, *107*(C12), 8014, doi:10.1029/2001JC001122.

Kraus, E. B., and J. S. Turner (1967), A one dimensional model of the seasonal thermocline. II The general theory and its consequences, *Tellus*, *19*, 98–106, doi:10.1111/j.2153-3490.1967.tb01462.x.

Lagerloef, G. S. E., G. T. Mitchum, R. B. Lukas, and P. P. Niiler (1999), Tropical Pacific near-surface currents estimated from altimeter, wind, and drifter data, *J. Geophys. Res.*, *104*, 23,313–23,326, doi:10.1029/1999JC900197.

Lagerloef, G., et al. (2008), The Aquarius/SAC-D mission: Designed to meet the salinity remote-sensing challenge, *Oceanography*, *21*, 68–81.

Lukas, R. (2001), Freshening of the upper thermocline in the North Pacific subtropical gyre associated with decadal changes of rainfall, *Geophys. Res. Lett.*, *28*, 3485–3488, doi:10.1029/2001GL013116.

Lukas, R., and E. Lindstrom (1991), The mixed layer of the western equatorial Pacific Ocean, *J. Geophys. Res.*, *96*, 3343–3357.

Maximenko, N. A., P. Niiler, M.-H. Rio, O. Melnichenko, L. Centurioni, D. Chambers, V. Zlotnicki, and B. Galperin (2009), Mean dynamic topography of the ocean derived from satellite and drifting buoy data using three different techniques, *J. Atmos. Oceanic Technol.*, *26*(9), 1910–1919, doi:10.1175/2009JTECHO672.1.

Mignot, J., and C. Frankignoul (2003), On the interannual variability of surface salinity in the Atlantic, *Clim. Dyn.*, *20*, 555–565.

Mignot, J., and C. Frankignoul (2004), Interannual to interdecadal variability of sea surface salinity in the Atlantic and its link to the atmosphere in a coupled model, *J. Geophys. Res.*, *109*, C04005, doi:10.1029/2003JC002005.

Niiler, P. P., and E. B. Kraus (1977), One-dimensional models, in *Modeling and Prediction of the Upper Layers of the Ocean*, edited by E. B. Kraus, pp. 143–172, Pergamon, New York.

Niiler, P. P., N. A. Maximenko, and J. C. McWilliams (2003), Dynamically balanced absolute sea level of the global ocean derived from near-surface velocity observations, *Geophys. Res. Lett.*, *30*(22), 2164, doi:10.1029/2003GL018628.

Ralph, E. A., and P. P. Niiler (1999), Wind-driven currents in the tropical Pacific, *J. Phys. Oceanogr.*, *29*(9), 2121–2129, doi:10.1175/1520-0485(1999)029<2121:WDCITT>2.0.CO;2.

Rao, R. R., and D. Sivakumar (2003), Seasonal variability of sea-surface salinity and salt budget of the mixed layer of the north Indian Ocean, *J. Geophys. Res.*, *108*(C1), 3009, doi:10.1029/2001JC000907.

Ren, L., and S. Riser (2009), Seasonal salt budget in the northeast Pacific Ocean, *J. Geophys. Res.*, *114*, C12004, doi:10.1029/2009JC005307.

Reverdin, G., E. Kestenare, C. Frankignoul, and T. Delcroix (2007), Surface salinity in the Atlantic Ocean (30°S–50°N), *Prog. Oceanogr.*, *73*, 311–340, doi:10.1016/j.pocean.2006.11.004.

Riser, S. C., L. Ren, and A. Wong (2008), Salinity in Argo: A modern view of a changing ocean, *Oceanography*, *21*, 56–67.

Roemmich, D., G. C. Johnson, S. Riser, R. Davis, J. Gilson, W. B. Owens, S. L. Garzoli, C. Schmid, and M. Ignaszewski (2009), The Argo Program: Observing the global oceans with profiling floats, *Oceanography*, *22*, 34–43, doi:10.5670/oceanog.2009.36.

Schmitt, R. W. (2008), Salinity and the global water cycle, *Oceanography*, *21*, 12–19.

Short, D. A., P. A. Kucera, B. S. Ferrier, J. C. Gerlach, S. A. Rutledge, and O. W. Thiele (1997), Shipboard radar rainfall patterns within the TOGA COARE IFA, *Bull. Am. Meteorol. Soc.*, *78*, 2817–2836, doi:10.1175/1520-0477(1997)078<2817:SRRPWT>2.0.CO;2.

Spall, M. A. (1993), Variability of sea surface salinity in stochastically forced systems, *Clim. Dyn.*, *8*, 151–160, doi:10.1007/BF00208094.

Wang, C., S. Dong, and E. Munoz (2010), Seawater density variations in the North Atlantic and the Atlantic meridional overturning circulation, *Clim. Dyn.*, *34*, 953–968, doi:10.1007/s00382-009-0560-5.

Webster, P. J., and R. Lukas (1992), TOGA COARE: The Coupled Ocean-Atmosphere Response Experiment, *Bull. Am. Meteorol. Soc.*, *73*, 1377–1416, doi:10.1175/1520-0477(1992)073<1377:TCTCOR>2.0.CO;2.

Wijesekera, H. W., C. A. Paulson, and A. Huyer (1999), The effect of rainfall on the surface layer during a westerly wind burst in the western equatorial Pacific, *J. Phys. Oceanogr.*, *29*, 612–632, doi:10.1175/1520-0485(1999)029<0612:TEOROT>2.0.CO;2.

Wunsch, C., P. Heimbach, R. Ponte, and I. Fukumori (2009), The global general circulation of the ocean estimated by the ECCO-consortium, *Oceanography*, *22*, 88–103, doi:10.5670/oceanog.2009.41.

Xie, P., P. Arkin, and J. Janowiak (2007), CMAP: The CPC merged analysis of precipitation, in *Measuring Precipitation from Space*, *Adv. Global Change Res*, vol. 28, edited by V. Levizzani, P. Bauer, and F. J. Turk, pp. 319–328, Springer, Dordrecht, Netherlands, doi:10.1007/978-1-4020-5835-6_25.

Yaremchuk, M. (2006), Sea surface salinity constrains rainfall estimates over tropical oceans, *Geophys. Res. Lett.*, *33*, L15605, doi:10.1029/2006GL026582.

Yin, X., A. Gruber, and P. A. Arkin (2004), Comparison of the GPCP and CMAP merged gauge-satellite monthly precipitation products for the period 1979–2001, *J. Hydrometeorol.*, *5*, 1207–1222, doi:10.1175/JHM-392.1.

Yu, L. (2006), Surface heat and freshwater fluxes, in *CLIVAR/GODAE Meeting on Ocean Synthesis Evaluation*, 29 pp., ECMWF, Reading, U. K. [Available from http://www.clivar.org/organization/gsop/synthesis/synthesis.php.]

Yu, L. (2007), Global variations in oceanic evaporation (1958–2005), Role of the changing wind speed, *J. Clim.*, *20*(21), 5376–5390, doi:10.1175/2007JCLI1714.1.

Yu, L., and X. Jin (2011), Satellite-based global ocean vector wind analysis by the Objectively Analyzed Air-sea Fluxes (OAFlux) Project: Establishing consistent vector wind time series from July 1987 onward through synergizing microwave radiometers and scatterometers, *WHOI OAFlux Tech. Rep. WHOI-OA-2011-01*, Woods Hole Oceanogr. Inst., Woods Hole, Mass.

Yu, L., and R. A. Weller (2007), Objectively Analyzed air-sea heat Fluxes (OAFlux) for the global ocean, *Bull. Am. Meteorol. Soc.*, *88*(4), 527–539, doi:10.1175/BAMS-88-4-527.

Yu, L., X. Jin, and R. A. Weller (2007), Annual, seasonal, and interannual variability of air–sea heat fluxes in the Indian Ocean, *J. Clim.*, *20*, 3190–3209, doi:10.1175/JCLI4163.1.

Yu, L., X. Jin, and R. Weller (2008), Multidecade global flux datasets from the Objectively Analyzed Air-sea Fluxes (OAFlux) Project: Latent and sensible heat fluxes, ocean evaporation, and related surface meteorological variables, *OAFlux Proj. Tech. Rep. OA-2008-01*, 64 pp., Woods Hole Oceanogr. Inst., Woods Hole, Mass.

L. Yu, Department of Physical Oceanography, Woods Hole Oceanographic Institution, MS 21, Woods Hole, MA 02543, USA. (lyu@whoi.edu)